Nuclear Engineering and Technology xxx (xxxx) xxx

Contents lists available at ScienceDirect

Nuclear Engineering and Technology

journal homepage: www.elsevier.com/locate/net

Original Article

Localization of hotspots via a lightweight system combining Compton imaging with a 3D lidar camera

Mattias Simons [a,*], David De Schepper [b,c], Eric Demeester [b,c], Wouter Schroeyers [a]

[a] Uhasselt – Hasselt University, CMK, NuTeC, Nuclear Technology- Faculty of Engineering Technology, Agoralaan H, 3590, Diepenbeek, Belgium
[b] KU Leuven, ACRO, Department of Mechanical Engineering, Wetenschapspark 27, 3590, Diepenbeek, Belgium
[c] Core Lab ROB, Flanders Make @ KU Leuven, Belgium

ARTICLE INFO

Keywords:
Compton imaging
Gamma camera
Decommissioning
Timepix3

ABSTRACT

Efficient and secure decommissioning of nuclear facilities demands advanced technologies. In this context, gamma-ray detection and imaging are crucial in identifying radioactive hotspots and monitoring radiation levels. Our study is dedicated to developing a gamma-ray detection system tailored for integration into robotic platforms for nuclear decommissioning, offering a safe and automated solution for this intricate task and ensuring the safety of human operators by mitigating radiation exposure and streamlining hotspot localization.

Our approach integrates a Compton camera based 3D reconstruction algorithm with a single Timepix3 detector. This eliminates the need for a second detector and significantly reduces system weight and cost. Additionally, combining a 3D camera with the setup enhances hotspot visualization and interpretation, rendering it an ideal solution for practical nuclear decommissioning applications.

In a proof-of-concept measurement utilizing a 137Cs source, our system accurately localized and visualized the source in 3D with an angular error of 1° and estimated the activity with a 3% relative error. This promising result underscores the system's potential for deployment in real-world decommissioning settings. Future endeavors will expand the technology's applications in authentic decommissioning scenarios and optimize its integration with robotic platforms.

The outcomes of our study contribute to heightened safety and accuracy for nuclear decommissioning works through the advancement of cost-effective and efficient gamma-ray detection systems.

1. Introduction

Decommissioning activities are expected to increase as more nuclear sites end their operational life [1]. An essential step in the decommissioning process of a nuclear site is the characterization and localization of hotspots. Reliable knowledge about radioactive contaminations and hotspots is necessary to execute future decommissioning steps. Localization of radioactive sources or hotspots is a primary concern during these operations or activities because early detection of hotspots allows for removing or taking early measures. This makes it possible to keep the operator dose uptake as low as possible, which is considered a good practice of maintaining it as low as reasonably achievable (ALARA) [2].

The current practice of localizing hotspots is for human operators to localize and characterize these hotspots manually. This is typically achieved through repetitive measurements using handheld detectors. However, this method is (1) labor-intensive, (2) it may expose operators to hazardous situations and high radiation doses, (3) it is prone to human mistakes, and (4) the hotspot location accuracy is limited.

Instead of relying on manual measurements by human operators, our research proposes a solution that can be integrated into our Archer robotic platform. The Archer mobile manipulator was developed to automate hotspot localization, making it an ideal candidate for nuclear decommissioning activities [3]. This robotic platform streamlines the repetitive measurements required for hotspot localization. The Archer robotic platform was successfully employed in our previous research [4]. It was equipped with a conventional CZT (Cadmium Zinc Telluride) detector to scan surfaces and identify hotspots.

The duration of each measurement step was optimized throughout the Archer project's implementation to minimize the total measurement time. However, while essential, the laborious process of step-by-step surface scanning poses potential challenges. Using probes or other

* Corresponding author.
E-mail address: mattias.simons@uhasselt.be (M. Simons).

https://doi.org/10.1016/j.net.2024.03.020
Received 12 December 2023; Received in revised form 22 February 2024; Accepted 17 March 2024

components near a hotspot can lead to contamination. Additionally, it's essential to acknowledge that advanced robotic platforms offer effective but relatively expensive solutions, which may not always align with the complex and dynamic nature of nuclear decommissioning environments.

To address these challenges, our research explores a proactive approach. This approach includes anticipating contamination hotspots, allowing the measurement strategy to be tailored to areas where contamination is likely, thus accelerating the measurement process and enhancing worker safety. Furthermore, this work highlights the potential benefits of integrating gamma cameras into robotic platforms, enabling remote measurements, reducing the risk of detector contamination, and making such systems more accessible to a broader range of applications.

Even without robotic platforms, gamma cameras have garnered significant attention within the nuclear field. Gamma cameras possess the inherent advantage of remote source localization. This attribute positions gamma cameras as highly intriguing tools for the nuclear industry, primarily allowing for enhanced worker safety through increased distances from potential radiation sources. Furthermore, gamma cameras often require minimal operator presence during measurements, contributing to the reduction of operator radiation exposure [4].

Gamma cameras can be classified into three categories based on their working principles: pinhole collimator [5], coded aperture [6], and Compton [7–9]. Each of these has its set of advantages and disadvantages. Typically, pinhole collimators and coded apertures offer better resolution, but they require a collimator that adds extra weight to the system and limits the field of view. On the other hand, Compton cameras do not require a physical collimator and can have a wider field of view, but they are unsuitable for energies below 250 keV [10].

However, it is essential to recognize that some commercial instruments measure the dose rate at the camera's location without considering the source-to-detector distance and only locate a source in 2D coordinates. Such devices are limited to finding the source in 2D coordinates. Unfortunately, this restriction makes it impossible to accurately estimate the source's activity. A source farther away from the detector would exhibit a significantly different activity level than one closer to the system despite generating the same measured dose rate.

For commercial gamma cameras that feature radiological and optical sensors such as [6,7], the challenge of parallax errors arises between the two types of images. Often, it is needed to manually correct parallax errors, which can involve assigning an average source-to-detector distance using a single distance sensor. However, this correction can introduce various errors, highlighting it as a prominent challenge for gamma cameras [11].

Paradiso et al. [12] introduced a stereo gamma camera to address this challenge. The method involves using two gamma cameras and coded masks combined with a 3D camera. The distance to the source is estimated using triangulation utilizing the pair of aligned gamma cameras. However, this approach faces the challenge of having a limited field of view and is relatively heavy and expensive due to the requirement for two separate gamma imaging systems.

However, as previously mentioned, Compton cameras do not require shielding, collimators, or coded masks, which often increase weight and limit the field of view. As a result, Compton cameras provide a substantially more extensive field of view, extending up to four-pi steradians,

The fundamental principle behind the Compton camera concept involves reconstructing Compton scattering events resulting from incoming gamma rays. Typically, the camera incorporates two or more position and energy-sensitive detectors. The initial sensor facilitates Compton scattering of incoming gamma rays, recording the location and energy of the recoiled electron. The scattered gamma ray continues to the second detector, where it gets absorbed. Applying the Compton scattering equation's kinematics, the angle at which the incoming gamma ray struck the detector can be precisely determined.

A significant advancement in lightweight Compton camera technology emerged in 2020 when D. Turecek [13] proposed the single-layer Compton camera based on Timepix3. This development reduces system weight and cost by obviating the need for a second detector.

This paper introduces an approach that realizes a Compton camera based 3D reconstruction algorithm with a single Timepix3 detector. Doing so eliminates the need for a second detector, significantly reducing system weight and cost. The Compton camera was also seamlessly integrated with a 3D camera that generated a 3D point cloud. This offers spatial information, enabling improved visualization and hotspot interpretation.

Our method further addresses the issue of parallax errors when coupled with a 3D camera, making it a well-suited solution for practical applications in decommissioning scenarios.

To prepare for real-life measurements in decommissioning scenarios, in-situ tests have been conducted under laboratory conditions, projecting radiological data onto the point cloud generated by the 3D camera. This approach enabled a more accurate estimation of source locations within the environment and enhanced hotspot visualization and interpretation.

Our method delivers a more cost-effective and lightweight Compton camera solution and offers valuable advantages when used with a 3D camera.

2. Materials and methods

2.1. Overview of the measurement setup

To develop a cost-effective and lightweight Compton camera, our method combines the functions of the scatterer and absorber layers of the Compton camera in one single layer. An Intel RealSense L515 lidar camera is integrated into the measurement setup to map the environment in 3D point clouds, adding spatial information to the radiological data processing.

The measurement setup is (see Fig. 1) mounted on an in-house developed pan-tilt unit to control the orientation of the Compton camera. The unit includes two stepper motors to control the setup's direction, a 3D-printed mount for the detectors and motors, and a Raspberry Pi to control the two stepper motors.

2.2. Detector design

In contrast to conventional Compton cameras utilizing two detectors, our research employs a single position-sensitive sensor, the Timepix3. A 3D reconstruction algorithm calculates the height difference between the two interactions.

The Compton camera consists of a Timepix3 detector, particularly

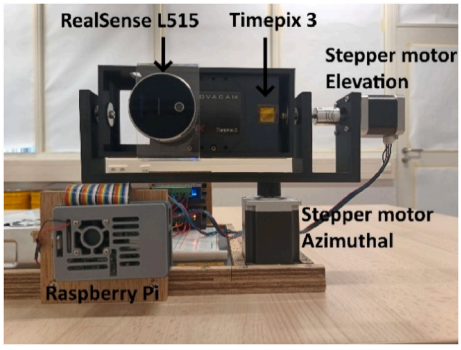

Fig. 1. Setup of the measurement system consisting of a Compton camera and a 3D camera mounted on a 3D-printed holder that can rotate around the axis of the Compton camera.

the Advapix TPX3 model purchased from Advacam. This 2D position-sensitive sensor comprises 256 by 256 pixels and can simultaneously register energy and time-of-arrival [14]. The detector utilizes a CdTe crystal with an area of 14 mm by 14 mm and a thickness of 1000 μm.

To perform Compton imaging, a Compton interaction, and photoelectric absorption are required to collect the total energy from the incident gamma ray. Subsequently, a cone is reconstructed, representing the gamma ray's possible origins. The cone's central axis is calculated using the coordinates of these two interactions, and the opening angle of the cone is calculated using Equation (1):

$$\cos\theta = 1 - \frac{m_e c^2 E_1}{(E_0 - E_1)E_0} \quad (1)$$

Where E_1 is the energy of the first interaction, E_0 is the energy of the incoming gamma rays, θ the opening angle of the cone, m_e is the mass of the electron, and c is the speed of light. Replicating this process and generating multiple cones allows for the intersection of these cones to pinpoint the source location [15].

Upon gamma ray interaction with the crystal of the Timepix3 detector, a cluster of hit pixels is formed due to the charge-sharing effect. After the measurement, a multistep process is employed to calculate these intersections of cones. Fig. 2 illustrates a flowchart detailing the reconstruction process. This process includes event selection, the 3D reconstruction algorithm, the back-projection algorithm, and determining maximum points or hotspots. These steps will be discussed sequentially in the following sections: 2.3 will discuss the preprocessing steps, 2.4 will discuss the back projection steps, 2.5 will discuss visualization, and 2.6 will discuss how activities are calculated.

2.3. Preprocessing

2.3.1. Clustering

After completing a measurement, the Pixet Pro clustering plugin [16] is used to group adjacent pixels into clusters and combine simultaneously interacting clusters into frames within the same 100 ns coincidence window.

Next, a spectrum is generated to identify energy peaks in the data. This spectrum aids in defining a region of interest of +- FWHM (full-width half maximum) of the measured peak.

2.3.2. Internal X-ray fluorescence (XRF) correction

After the clustering step, a correction for internal X-ray fluorescence (XRF) is applied. Internal XRF in the CdTe sensor can occur when a gamma ray excites Cd or Te atom. Then, an XRF photon is emitted that can be detected in another pixel.

As a consequence, the energy of the original cluster is decreased by the energy of this XRF photon, and an additional cluster is created. This distorts the collected energy and creates an additional cluster. The XRF cluster must be corrected to avoid interference with the information needed for Compton imaging. Following the approach proposed in Ref. [17], all clusters with energy in a 10–40 keV window within 10 pixels from another cluster are removed, and the energy is added to the nearest cluster.

Table 1
Characteristic X-ray energies of Cd and Te [18].

Element	Z	Kα1 (keV)	Kα2 (keV)	kβ1 (keV)
Cd	48	23.17	22.98	26.06
Te	52	27.47	27.20	31.70

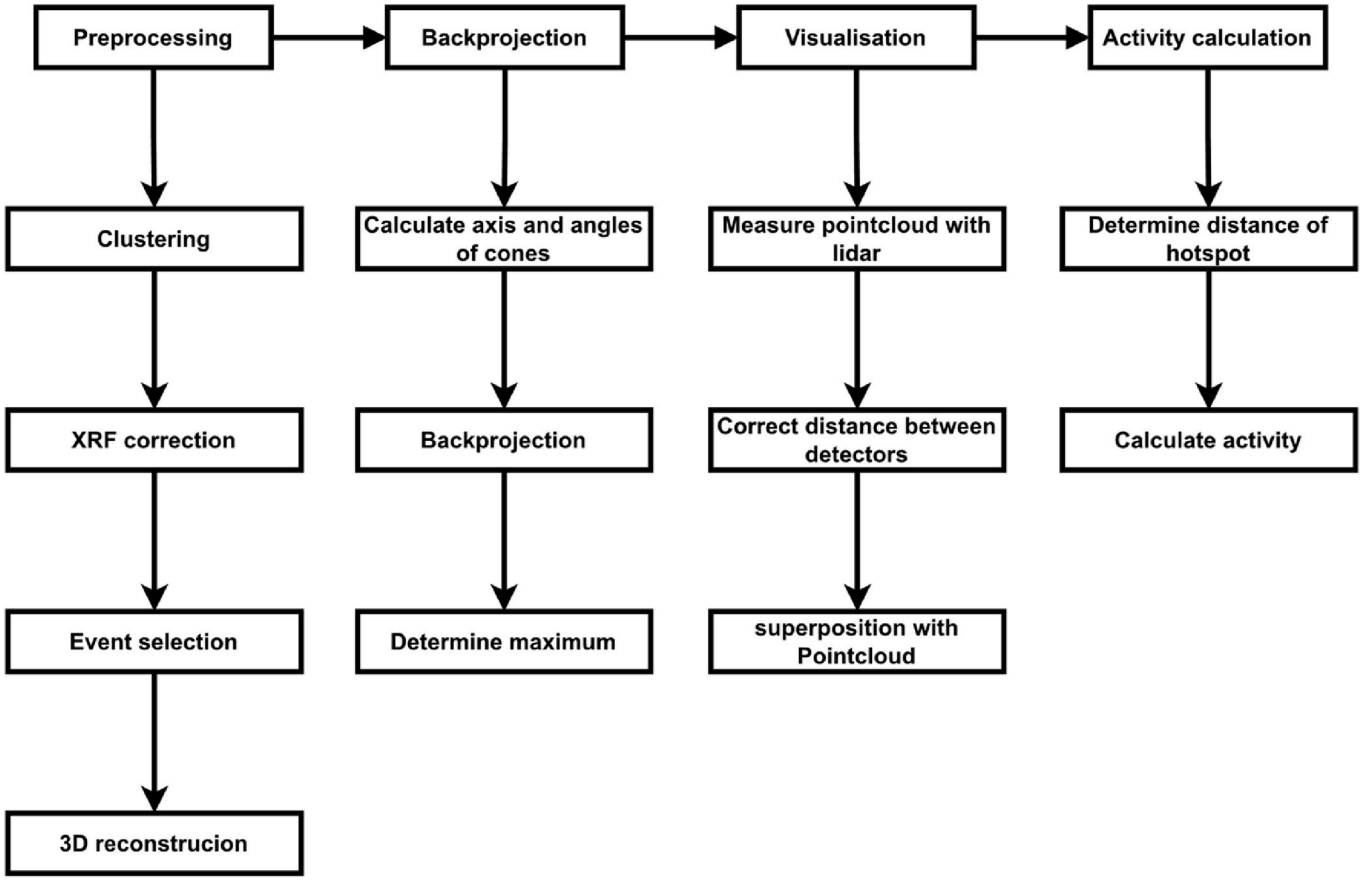

Fig. 2. Flowchart of the multistep process used for gamma-ray detection.

Table 1 provides the characteristic X-ray energies of Cd and Te, guiding the XRF correction process. After this correction, frames suitable for reconstruction are selected.

2.3.3. Event selection

Our study identifies cones based on the central axis and the opening angle, requiring specific conditions for frame selection:

- The frame must contain two clusters.
- The total energy should match one of the gamma peaks within a plus or minus one FWHM range.

These conditions suggest that one cluster results from Compton scattering, while the other is due to photoelectric absorption, and all the energy from the incident gamma is detected in the sensor. If these conditions apply, the frame is deemed suitable for subsequent analysis.

2.3.4. 3D reconstruction algorithm

Next, a 3D reconstruction algorithm is applied for all suitable frames. An interaction's x and y position in the detector can be obtained directly from the pixel's location. However, the vertical depth (z) is determined differently to improve the uncertainty on the central axes of the cone. To achieve this improvement, a 3D reconstruction algorithm is used to estimate the height difference between the two interactions based on the difference in arrival time between the two events in coincidence. Because the Timepix3 chip can measure arrival time with a resolution of 1.6 ns, it is possible to measure differences in the collection time of different events.

Due to the small pixel size compared to the thickness of the sensor, also known as the small pixel effect, the significant contribution of the induced signal is created when the charge has drifted to the proximity of the pixel electrodes. A principle similar to a time projection chamber 3D track reconstruction can be performed.

Bergman et al. already demonstrated the 3D particle track capabilities of Timepix3 detectors with silicon [19] and CdTe [20]. However, their calibration procedure used muons generated at SPS at CERN. Cosmic muons could be used to perform this calibration. However, it requires measuring the natural background for a long time. To avoid repeating the prolonged background measurement, we opted to simplify the method and, in a later step, verify it by measuring cosmic muons.

In our approach, the electric field (E) is assumed to be homogeneous and is calculated as a constant value using Equation (2):

$$E = -300\ V / 1000\ \mu m \tag{2}$$

Where 300 V is the bias voltage and 1000 μm the thickness of our crystal, the drift velocity (v_e) is assumed constant and calculated using Equation (3).

$$v_e = -\mu_e \times E \tag{3}$$

Where μ_e is the electron mobility, and E is the electric field. Typical electron mobilities for CdTe crystals measured between 1000 and 1100 $cm^2V^{-1}s^{-1}$ [21,22]. The resulting drift velocity (33 μm/ns) is used in Equation (4) to calculate the difference in height between pixels.

$$\Delta z = \Delta t \times v_e \tag{4}$$

Where Δz is the difference in height between pixels, and Δt is the difference in time-of-arrival in nanoseconds.

As verification, lookup tables are also generated with cosmic muons using the method proposed in Ref. [20]. Fig. 3 shows a plot of the generated lookup table. This table was then approximated with the least square linear fit shown in Equation (5):

$$z = 46.43 + 32.27\ t \tag{5}$$

In our case, the constant value of 46.43 would not influence the measurement as the normalized vector between the two interactions is needed for the cone's central axis.

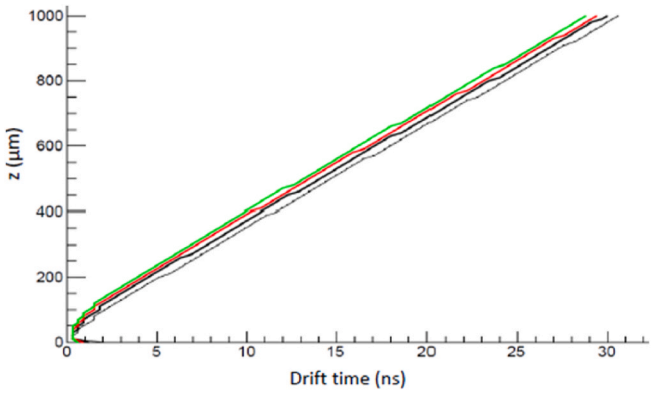

Fig. 3. A plot of the generated lookup tables for four energy bins of 25 keV; the grey line has an energy bin of 0–25 keV, the black line from 25 to 50 keV, the red from 50 to 75 keV and the green line has an energy bin of 75–100 keV. (For interpretation of the references to color in this figure legend, the reader is referred to the Web version of this article.)

A cosmic muon event was reconstructed to visualize the capabilities of the 3D reconstruction algorithm. In a muon event, all points should be in a straight line. Pixels with registered energy lower than 30 keV are corrected for the time-walk effect, and afterward, the depth of the interaction is reconstructed.

Fig. 4 shows the 3D scatterplot of the reconstructed pixels from the cosmic muon. After the reconstruction of the Z coordinate, the least square fit of a straight line is made with an R^2 value of 0.862.

2.4. Back-projection

2.4.1. Calculate angles and axes

The coordinates of the central axes are calculated as the weighted mean of the coordinates of every pixel in that cluster. This weighing was based on the energy deposited in each pixel.

To calculate the opening angle and direction of the cone, understanding which cluster resulted from the Compton interaction and the photoelectric absorption is crucial. In a typical Compton camera with a

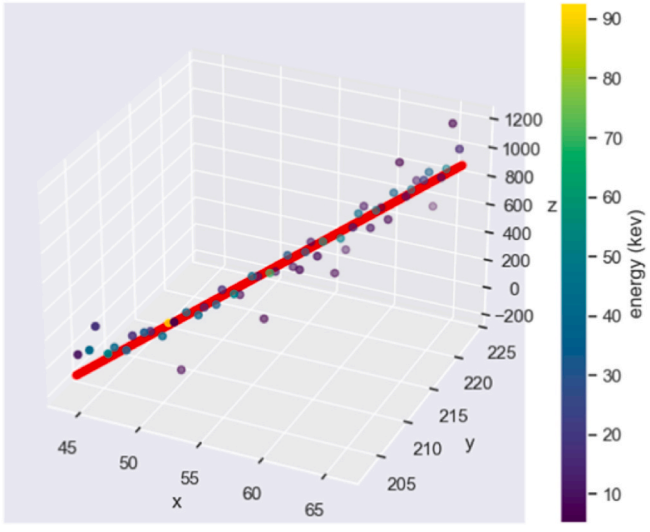

Fig. 4. 3D scatterplot of a reconstructed muon, fitted by a straight line with an R^2 value of 0.862. The color of the points represents the deposited energy in the pixel. (For interpretation of the references to color in this figure legend, the reader is referred to the Web version of this article.)

low Z scatterer and high Z absorber, the assumption is often made that the Compton scattering occurs in the first detector. However, our setup presents a challenge where both interactions occur in the same detector. In specific cases, it is possible to determine the Compton interaction, particularly when one of the interactions exceeds the maximum energy that can be deposited by Compton scattering.

However, when measuring ^{137}Cs, most of the time, this is not possible. For these cases, both options are considered for every pair of interactions: One cone where the right cluster was considered the Compton event, and the other where a wrong cone was generated with a faulty opening angle and at the wrong side of the central axis. It was assumed that the noise of a faulty cone is spread out over the four-pi field of view and will not significantly impact the image at the location of the source.

2.4.2. Back-projection algorithm

Next, all cones were fed to a direct back-projection algorithm in spherical coordinates. The maximum is determined, and the number of overlapping cones is counted at this maximum. Fig. 5 shows an illustration of 4 intersecting cones on a spherical surface.

In summary, the gamma-ray detection and 3D reconstruction process involves a multi-step approach, including clustering, event selection, XRF cluster correction, and depth reconstruction to determine the central axis and opening angle to generate a cone of possible source locations. These cones are then fed to a direct back-projection algorithm in spherical coordinates, the maximum is determined, and overlapping cones are at the maximum.

2.5. Visualization

2.5.1. Measuring point cloud

After the radiological measurement with the Compton camera, a point cloud of the environment is measured while the setup remains in the same orientation. For this, a RealSense L515 camera (Intel Corporation) captured RGBD images. This camera has a field of view of 70° by 55° and uses a laser to determine the distance using Time-of-Flight technology. It has a range of up to 9 m with an accuracy of + - 3% and features a maximum resolution of 1024 × 768 pixels at 30fps. This camera was also chosen because of its lightweight and small size, with a diameter of 61 mm and height of 26 mm, making it suitable for mounting on the measurement setup next to the Compton camera.

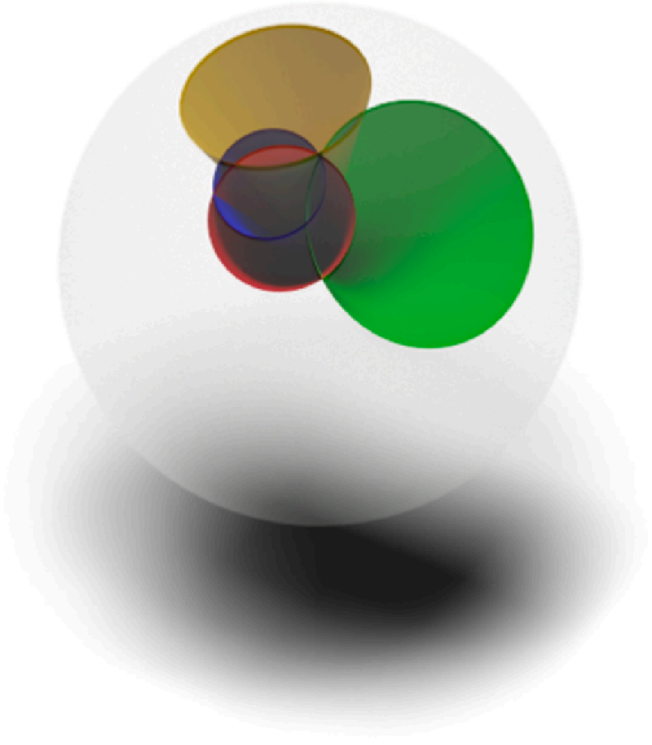

Fig. 5. An illustration of four cones that are back-projected on a sphere. Each cone (red, green, yellow, and blue) results in a circle on the sphere's surface. (For interpretation of the references to color in this figure legend, the reader is referred to the Web version of this article.)

2.5.2. Distance correction and superposition

However, before the radiological data and the point cloud can be superimposed, the measured point cloud needs to be transformed to match the coordinate system of the Compton camera. To do this, the physical distance was measured between the two cameras, and all 3D points are transformed according to this. After this correction, the Compton image is projected outwards, and points that overlap with the angles where a hotspot was found are marked.

2.5.3. Activity calculation

To estimate the activity of the source, it is essential to know the distance between the source and detector since the measured number of cones typically decreases by the distance squared. To determine this distance, the marked points are used to calculate the average distance between the Compton camera and the hotspot points. The activity is estimated with this distance by correcting for the distance squared by using Equation (6):

$$A = \frac{{r_2}^2 \times n}{{r_1}^2 \times t \times \varepsilon} \tag{6}$$

Where A is the activity, ε the efficiency, r_1 is the source-to-detector distance during the efficiency measurement, r_2 is the source-to-detector distance during the actual measurement, n is the number of overlapping cones, and t is the time. The uncertainty can then be estimated using Equation (7):

$$\frac{\Delta A}{A} = \sqrt{\left(\frac{\Delta \varepsilon}{\varepsilon}\right)^2 + \left(2\frac{\Delta r_2}{r_2}\right)^2 + \left(2\frac{\Delta r_1}{r_1}\right)^2 + \left(\frac{\Delta n}{n}\right)^2} \tag{7}$$

Where $\Delta\varepsilon/\varepsilon$ is the uncertainty on the efficiency, $\Delta r_2/r_2$ is the uncertainty on the source-to-detector distance, $\Delta r_1/r_1$ is the source-to-detector distance during the efficiency measurement, and $\Delta n/n$ is the uncertainty caused by the number of events.

2.6. Experimental procedure

The efficiency of the Compton camera was measured for different camera-source orientations, and the angular dependency of the efficiency was investigated. The measurement setup with the Compton camera and the 3D camera was rotated at intervals of 5° to obtain measurements from various angles. Each measurement was taken for 1 h to ensure sufficient statistics. A calibrated ^{137}Cs point source with an activity of 14.15 MBq ± 2.5% is placed 30 cm from the sensitive crystal of the detector.

Corrections were applied to the data measured by the Compton camera to account for various environmental factors, including the detector's operating temperature. These corrections involved measuring the energy spectrums and resolution of the camera for different gamma-ray energies at different temperatures. This was done using a known radioactive source with a well-defined gamma spectrum.

Various parameters were adjusted, and the resulting measurements were analyzed. These parameters included the angle between measurement setup and source and source-to-detector distance. The data was then processed using a multi-step approach. 3D point clouds were generated using the Intel Realsense L515 camera. This point cloud was superimposed with the Compton imaging data, and activities are

calculated.

The experimental procedure was conducted in a controlled laboratory environment to ensure accurate and reliable results.

2.7. Data analysis

In this paper, all software was written in Python 3.10. For all 3D visualizations, point-cloud manipulations, and mesh generating, open3D version 0.14.1 is used. This is an open-source library for 3D data [23]. PiXet Pro software version 1.7.8 was used to control and acquire data for the Timepix3 detector [24].

3. Calibrations and corrections

3.1. Time-walk effect correction

For the 3D reconstruction algorithm to determine the depth between interactions, precise time-of-arrival data is needed.

The time-walk effect describes the delay in detecting pulses with low energy (amplitude) compared to concurrent signals with high energy. For proper timestamping, this effect must be corrected. Pixels with low energy tend to suffer from a delay in the registration of the arrival time. A lower slope of the signal in the electronics causes this. The calibration can be performed in different ways, through injecting test pulses [25] or experimentally [24]. However, we opted for an experimental approach following the method described in Ref. [24] and further detailed in this section.

After a ^{241}Am source irradiates the sensor, all clusters where the sum of the deposited energies equals 59.5 keV are selected. All pixels in such a cluster are in coincidence even when they have different energies and arrival times. The clusters with a size of 3 or 4 pixels where one pixel has an energy equal to 30 keV are selected. This 30 keV pixel serves as a reference time, while the other pixels collect the remaining charge and share it according to the charge-sharing effect. The energy is binned in bins of 1 keV, and Gaussians fit the delay in arrival time for each energy bin. Their mean values are plotted as a function of energy, describing the time-walk dependence on energy. This is approximated by Equation (8), a non-linear function ΔT depending on parameters c, E0, and d:

$$\Delta T = c \Big/ (E - E0)^d \tag{8}$$

Where ΔT is the time-walk [ns], E is the pixel's energy [keV], the least-square fit determines E0, the detector threshold level, and c and d parameters.

Fig. 6 shows the time-walk graph and fit. As seen in the graph, the uncertainty increases as pixel energy gets closer to 5 keV (the threshold for the detector in our case), increasing the error on the reconstruction of the z-coordinate of the cone axis for low-energy pixels. The coordinates are weighted by energy deposited in the pixel to counter this phenomenon.

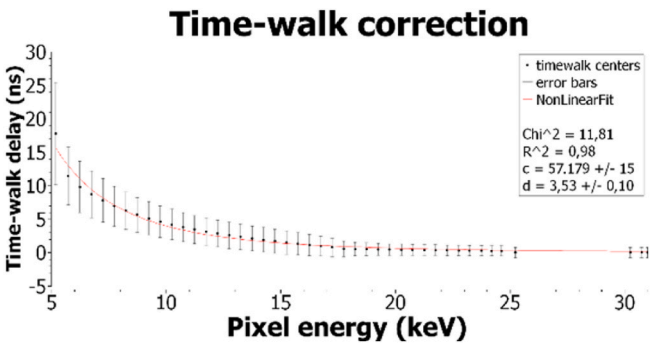

Fig. 6. In the time-walk correction graph, the measured pixels are binned in bins of their energy keV, and a Gaussian function fits each bin. On these Gaussians, a nonlinear function is fitted to correct for the time-walk effect.

3.2. Temperature correction

A study conducted on a Timepix3 detector with 300 μm Si as a sensitive crystal by Martin Urban [26] found no significant change in photon detection efficiency at different temperatures up to 80 °C. However, the accuracy is influenced by a change in operating temperature, and a shift in the spectrum towards higher energies can be seen. The research also showed that higher energies are more affected by increased temperatures.

The energy calibration of the detector was performed at 20° operating temperature. However, in the current enclosure on the measurement setup, the operating temperature ranges between 35 and 40° (the temperature was reported by Pixet Pro measurement software).

To compensate for this effect, a spectrum of ^{137}Cs, ^{152}Eu, and ^{241}Am was measured at two different temperatures, 20 and 40°. This resulted in a shift of three percent of the measured energies towards higher energies.

3.3. Efficiency calibration

Efficiency is an essential parameter for gamma-ray detectors as it indicates the fraction of gamma rays detected by the detector. A higher efficiency means more gamma rays are detected in the same measuring time, resulting in better statistics and more accurate measurements. It also allows an estimate of the activity of a source from a measurement. However, several factors can influence the efficiency of gamma-ray detectors, including the energy of the gamma-ray, thickness, material of the detector, geometry of the detector and source, source-to-detector distance, etc. Therefore, a well-known efficiency calibration is needed to 'accurately' estimate the activity of a source.

Different approaches have been proposed to model the efficiency of a detector in well-known geometries, such as Monte Carlo based approaches [27]. However, these often take a long time to model and need verification with experimental data and, most importantly, a well-known geometry. In the case of a Compton camera that is locating radioactive sources at unknown locations, having a well-known geometry up front is impossible. Therefore, an experimental approach is preferred, and the model was simplified [28].

To calculate efficiencies, it is assumed that all sources are point sources, which is an acceptable assumption as the active area of the source has a diameter of 10 mm compared to a distance of 30 cm for the efficiency calibration or ±4 m for the proof of concept measurement. The factors influencing the efficiency are separated into energy, incident angle, and distance.

The efficiency was determined for events that have two interactions that comply with the conditions to generate a Compton cone. This was done for intervals of 5° angle ranging from −55 to 55° for both azimuthal and longitudinal angles.

The point cloud was used to measure the distance to the source and was corrected for using the distance squared.

In this paper, a ^{137}Cs course was used. However, this procedure can be repeated for other sources.

4. Results and discussion

This section presents the results of our lightweight Compton imaging system, which combines the functions of the scatterer and absorber layers into a single layer using a 3D reconstruction algorithm.

A proof of concept measurement is performed with a ^{137}Cs source with 14.15 MBq ± 2.5% activity. The source is located at a 3.95 m distance from the detector. A picture of the setup used for the proof of concept experiment is shown in Fig. 7. First, an example of an event will be discussed from the preprocessing step to the back-projection step of the method. After this, the efficiency is discussed, and finally, the

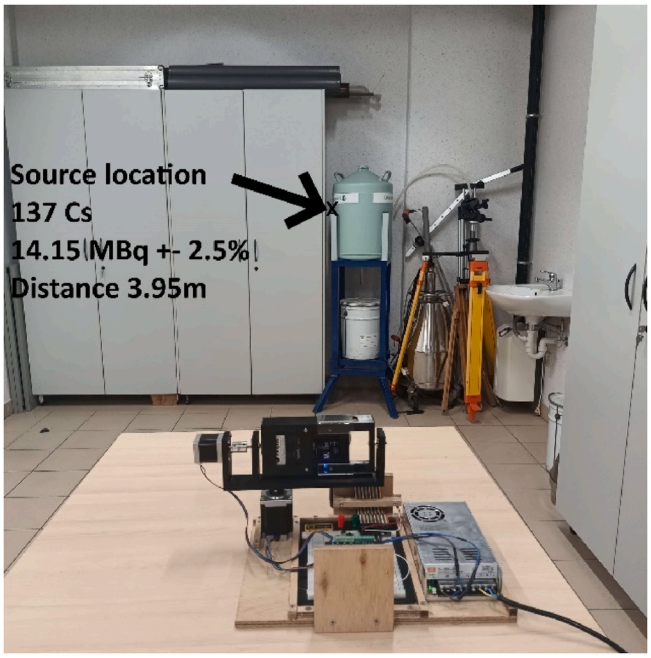

Fig. 7. Picture of the test setup. A 137Cs source is located at the small black cross indicated by the arrow 3.95 m from the detector.

measurement is superimposed with the 3D camera, and the activity is calculated.

4.1. Preprocessing and cone analysis

After completing the measurement, the preprocessing algorithm is employed, and suitable events are selected. Next, the possible Compton cones are made to determine the location of the gamma-ray source with the Compton camera.

The cones are created from two interactions. The axes are determined by the coordinates of the two interactions and the opening angle by the energy of the Compton interaction. However, in our case, it is unknown which of the two is the Compton interaction. Therefore, a cone is generated at both sides of the central axis, knowing that one of them is faulty.

This is illustrated by an example of two cones generated during a real-life measurement of ^{137}Cs. These cones are generated from an event that meets the criteria for event selection. Table 2 shows the normalized central axis (X, Y, and Z) and opening angle for two cones generated by an incident gamma ray. At the same time, the Energy column represents the energy of the interaction that was assumed to be the Compton event for the respective cone.

Fig. 8 shows the result of back-projecting the two respective cones in Table 2. In this case, the two cones are generated from the same event.

4.2. Back-projection

Fig. 9 presents the initial back-projection heatmap of the test setup derived from a modest number of cones (25 events resulting in 43 cones). The emerging spatial distribution provides an early glimpse of

Table 2
Normalized central axis coordinates (X, Y, and Z) and opening angle of two cones generated by an incident gamma ray. During the preprocessing steps, these clusters were identified to meet the criteria for Compton cone reconstruction.

Cone	X	Y	Z	Opening angle (°)	Energy (keV)
1	0.93	−0.34	0.12	94	395
2	−0.93	0.34	−0.12	62	277

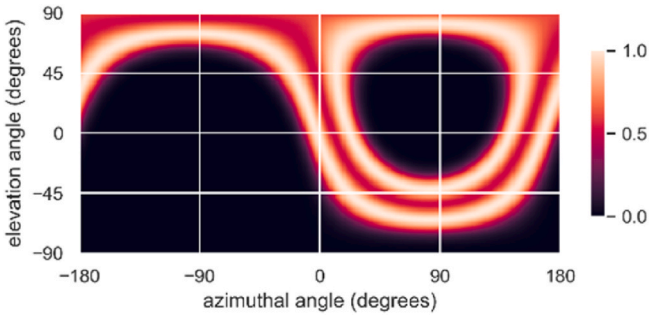

Fig. 8. A heatmap of the result of back-projecting two cones. The colors represent a value for each pixel based on the Gaussian overlap between the cone and that pixel. (For interpretation of the references to color in this figure legend, the reader is referred to the Web version of this article.)

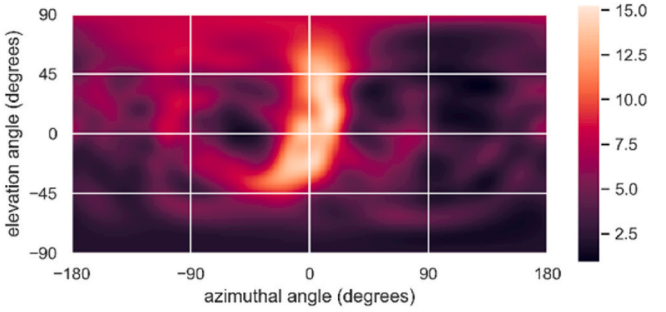

Fig. 9. The initial back-projection heatmap illustrates the spatial distribution resulting from a limited number of cones; the colors in the figure represent the sum of the Gaussian overlap of each back-projected cone. As the cones increase, the emerging pattern becomes more discernible. (For interpretation of the references to color in this figure legend, the reader is referred to the Web version of this article.)

the possible locations of the detected hotspot. The colors represent the sum of the Gaussian overlap of the cones with that pixel. A smeared-out bright spot is seen; however, the maximum in this figure at 14-degrees elevation and 15° azimuthal angle misses the actual location of the source with 20°. Subsequent figures will reveal the evolution of this pattern as more cones are incorporated into the reconstruction.

Building on the previous figures, Fig. 10 showcases the continued refinement of the back-projection heatmap by accumulating additional cones. The heightened clarity in the spatial distribution highlights the effectiveness of the back-projection process. This figure results from the back-projection of 100 events (180 cones). A single bright spot can be seen with the maximum at 1-degree elevation and 2° azimuthal angle, only missing the actual location with 2,2°.

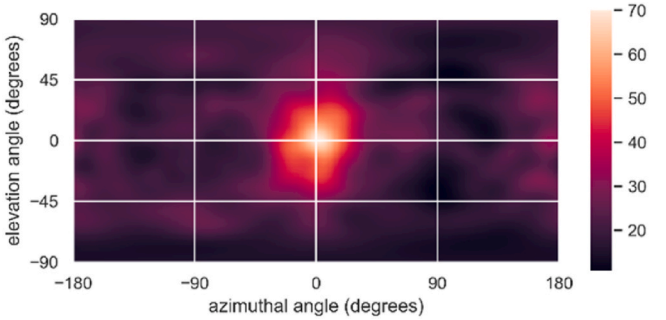

Fig. 10. A Continuing the accumulation of cones, Fig. 10 demonstrates a further refinement in the back-projection heatmap. The increasing number of cones continues to enhance the clarity of the spatial distribution.

Fig. 11 marks the end of the cone accumulation process of the 5-h test measurement, resulting in a comprehensive back-projection heatmap. The spatial features converge to deliver a detailed representation of the gamma-ray hotspot. During this time, 186 events were measured with 335 cones. The maximum was localized at 1-degree elevation and 0° azimuthal angle, missing the source by 1°.

4.3. Visualization

After the radiological measurement, the RealSense RGBD camera measures a point cloud of the environment. A mask is applied to the back-projection map so that only the segments on the sphere with the 1% highest overlap of cones remain. These spherical coordinates are projected to the point cloud, and the measurement is superimposed with the point cloud from the 3D camera. Points that fall in the sphere segments where the source is estimated are colored red in Fig. 12.

The black parts in the figure are parts where no depth could be measured. Multiple factors can cause this. For example, some surfaces do not reflect the laser to the lidar camera when the point is outside the field of view, or the laser is blocked.

After the superposition of the back-projection with the point cloud, the mean distance from all the points in the colored area was taken, and the efficiency was calculated for this distance.

After averaging the distance between the detector and the points in the point cloud within the hotspot region, the distance was calculated as 3.96 m, and the center point of the colored hotspot missed the exact location of the source by 10 cm.

After this, the create_from_point_cloud_poisson() function from open3d was used to generate a triangle mesh from the point cloud. The result is shown in Fig. 13. This helped to improve the clarity of the picture.

4.4. Activity calculation

This subsection discusses the results of estimating the activity. An efficiency calibration was made at intervals of 5° to do this.

Due to the flat rectangular shape of the detector's active area, it was anticipated that the incident angle of the radiation would affect the efficiency. Fig. 14 illustrates the efficiency results at 5-degree intervals within the field of view, spanning from −55 to 55° azimuthal angle and elevation angle. Fig. 14 portrays the fluctuation of the efficiency across both angles. Figs. 15 and 16 provide side views of the 3D scatterplot for a more detailed view.

Due to the rectangular shape of the detector's active area, it was estimated that the efficiency would be symmetric across both angles. However, an apparent asymmetry is observed across the azimuthal pitch of the system. An example of this is given in Table 3.

This asymmetry is likely caused by the aluminum cover for the sensor's readout electronics and the aluminum support bars that hold the sensor in place. However, in the elevation direction of the detector, the efficiency exhibits a symmetrical pattern.

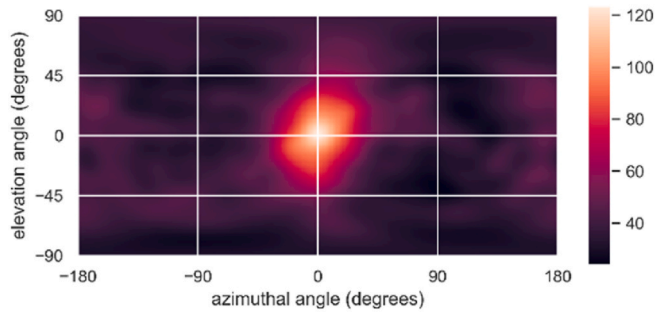

Fig. 11. The cones of the entire 5-h measurement are accumulated, resulting in a comprehensive back-projection heatmap.

Fig. 12. The front view of the four-pi Compton camera image is superimposed with the point cloud. A mask is applied to display only the top 1% of the highest radiological values, and the hotspot location is highlighted in red. (For interpretation of the references to color in this figure legend, the reader is referred to the Web version of this article.)

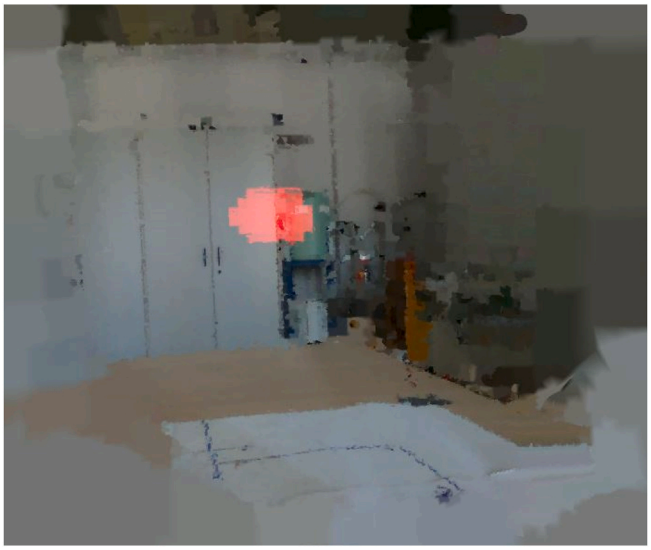

Fig. 13. A picture of the generated triangle mesh from the point cloud to improve the clarity. The hotspot is indicated in red. (For interpretation of the references to color in this figure legend, the reader is referred to the Web version of this article.)

A lookup table for efficiency was created to estimate the efficiency at an unknown angle, and linear interpolation was used between data points.

In the case of the example measurement, the hotspot was located at 1-degree elevation and 0° azimuthal angle. At this point, interpolation was employed to estimate the efficiency.

After interpolation, it was expected that 4653 overlapping cones would be observed during a 1-h measurement of a 14.15 MBq ^{137}Cs source at a 30 cm source-to-detector distance. A 1 MBq source at 30 cm should yield approximately 328.8 cones per hour. During the 5 h

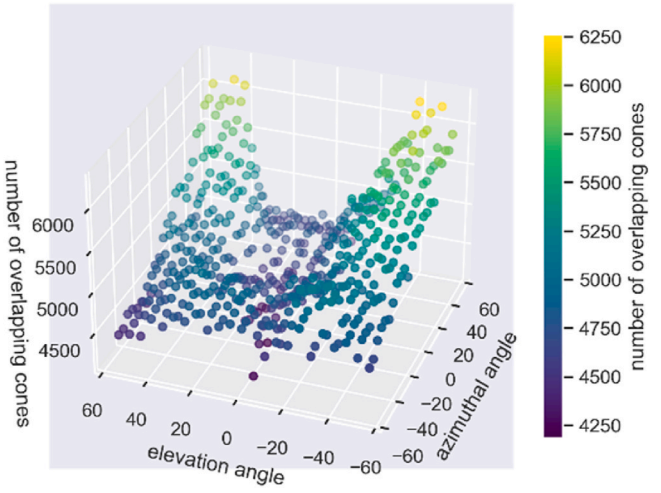

Fig. 14. A 3D scatterplot demonstrating the efficiency of the detector. The elevation axis and azimuthal axis represent the orientation of the detector. The scatterplot visually illustrates the efficiency across different detector orientations, providing valuable insights into the detector's performance variation. The figure's color scale and Z-axis represent the number of overlapping cones at the hotspot location that were measured during the 1-h efficiency measurement. (For interpretation of the references to color in this figure legend, the reader is referred to the Web version of this article.)

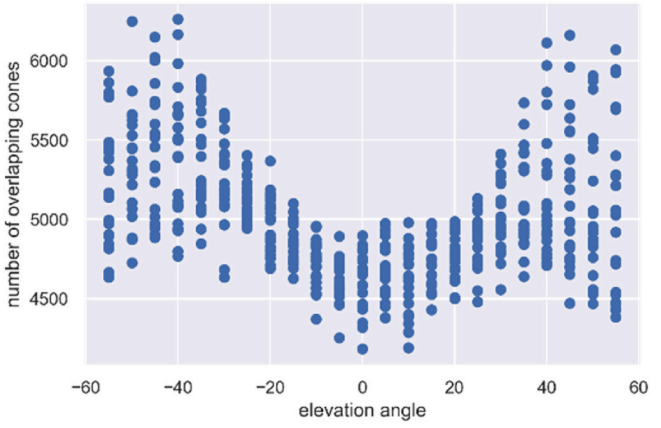

Fig. 15. A scatterplot that provides a side view of Fig. 14 across the elevation angle. Along the elevation axis, a symmetry can be observed.

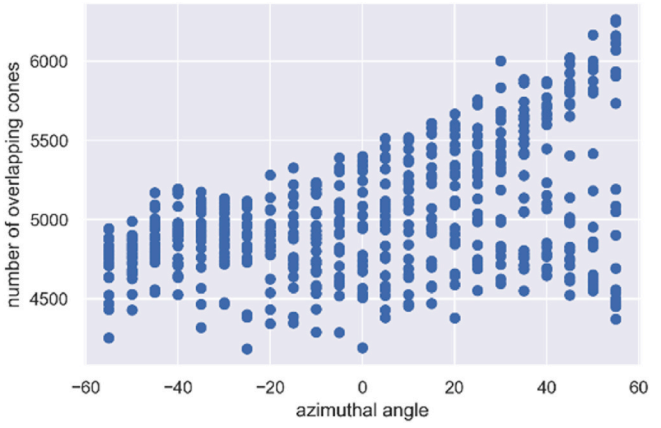

Fig. 16. A scatterplot provides a side view of Fig. 14 across the azimuthal angle. In this direction, the efficiency is asymmetrical.

Table 3
Example of the number of overlapping cones at different orientations.

Angle	Elevation −50°	Elevation 50°
Azimuthal −50°	4586	4527
Azimuthal 50°	5810	5875

measurement, 138 cones were detected at the hotspot location. Using Equation (6), the activity was calculated as 14.62 MBq. This represents a relative difference of 3 percent.

The uncertainty of the calculated activity is approximated to be 9.7% using Equation (7):

Table 4 shows an estimate of the uncertainty of several factors. The uncertainties on the efficiency $\Delta\varepsilon/\varepsilon$ and number of overlapping cones $\Delta n/n$ are based on the number of counts. The datasheet of the RealSense L515 reported the 3% uncertainty of the distance $\Delta r2/r2$, and the 1% uncertainty of the distance during the efficiency measurement is based on the measurement error, which was about 3 mm on 30 cm distance.

However, it is essential to acknowledge that the source must be located on the environment's surface. Due to the lidar, the distance of sources hidden behind other objects is not reported correctly, and therefore, it is impossible to estimate an activity accurately.

4.5. Comparison with previous studies

Our findings are consistent with Turecek's 2019 work [12], particularly in adopting the single-layer Compton camera design. However, our study extends beyond this framework, incorporating crucial enhancements that contribute to advancing gamma-ray imaging technology. Notably, a meticulous efficiency calibration procedure was performed, a critical step in ensuring the accuracy and reliability of our results. Furthermore, integrating a 3D camera into our setup provides a spatial dimension that enhances the visualization and interpretation of radiological data.

One of the distinctive features of our research lies in the ability to calculate activities, a capability that extends the practical applications of our Compton camera. This represents a significant stride toward real-world utility, enabling the estimation and analysis of radioactive source activities in diverse settings. These supplementary elements validate our findings against Turecek's groundwork and position our study as a comprehensive contribution to gamma-ray imaging.

Our setup weighted 0.6 kg, which included the Timepix3 detector and RealSense 3D camera. The stepper motors are not included in the weight, as these were only used to automate the positioning of the setup during the efficiency measurements.

In comparing the intrinsic efficiency of our system, 4.54×10^{-4}, stands in the range with that of Rena mini™ long (Kromek), another lightweight system [9]. Despite the similarities in intrinsic efficiency, our system demonstrates an advantage in precision, as shown in Table 5.

However, our system implemented the direct back-projection algorithm, which yielded an image resolution expressed as Full Width at Half Maximum (FWHM) of 50° compared to the 10° FWHM reported by Ref. [9]. Therefore, it is essential to acknowledge that further enhancements to increase the resolution can be achieved, for example, by implementing deconvolution or more advanced reconstruction algorithms.

5. Conclusion

In conclusion, this research introduced an innovative lightweight

Table 4
Uncertainties influencing the activity estimation.

$\Delta A/A$	$\Delta\varepsilon/\varepsilon$	$\Delta r_2/r_2$	$\Delta r1/r1$	$\Delta n/n$
9.7%	1.5%	3%	1%	8.5%

Table 5
Source position of reconstructed images and errors of Rena mini™ long [9] compared to our system.

The offset angle of the source	located position Rena mini™ long [9]	Error Rena mini™ long [9]	located position Our system	Error Our system
0°	0°	0°	1°	1°
10°	9°	1°	10°	0°
20°	16.2°	3.8°	21°	1°
30°	27°	3°	31.4°	1.4°
40°	32.4°	7.6°	41.4°	1.4°

measurement approach to enhance the efficiency and practicality of gamma-ray detection for nuclear decommissioning and other applications. Combining a Compton camera based 3D reconstruction algorithm with a single Timepix3 detector successfully eliminated the need for a second detector, substantially reducing system weight and cost.

Our approach improves spatial information and visualization capabilities by integrating our lightweight Compton camera with a lightweight 3D camera. This enabled hotspot visualization and interpretation while minimizing the impact of parallax errors. Additionally, it allows for an accurate estimate of the source-to-detector distance, which is an essential factor in estimating the activity of the source.

Also, our study investigated the angular dependency of the efficiency of our Compton camera. Through experimental calibration, the efficiency of our system was determined, giving insight into its performance across different orientations relative to the gamma-ray source. This investigation contributes to understanding the system's behavior and allows for accurately estimating source activities.

During our test measurements, our lightweight setup of only 0.6 kg could localize and estimate the activity of a point source with a 3% relative difference at a distance of 3.95 m from the detector.

Our findings also emphasize the potential applications of this technology in the context of robotic systems used for nuclear decommissioning. Automation, enabled by such advanced gamma-ray detection solutions, offers the opportunity to safeguard human operators by minimizing radiation exposure and streamlining hotspot localization.

Our study's results advance nuclear decommissioning processes and hold promise for other fields, such as medical imaging, nuclear security, and environmental monitoring. As the need for efficient gamma-ray detection continues to grow, our approach represents a significant step towards enhancing safety and accuracy in various applications. It provides a valuable foundation for developing more cost-effective and efficient gamma-ray detection systems, potentially revolutionizing how to address the challenges of nuclear decommissioning.

Moving forward, research should focus on expanding the practical applications of this technology in real-world decommissioning settings, further optimizing the integration of Compton cameras with robotic platforms. Additionally, further investigation should be performed into using more advanced Compton reconstruction algorithms to improve the resolution.

Declaration of competing interest

The authors declare no conflicts of interest regarding the publication of this manuscript. The research presented in this paper was conducted with academic and scientific integrity. There are no financial, personal, or professional relationships that could be perceived as potential conflicts of interest. This manuscript has not been submitted to any other journal for simultaneous consideration. We confirm that this work is original and has not been published elsewhere.

Acknowledgements

This work was also supported by the Research Foundation - Flanders (FWO) scholarship nr 1SA2621N and 1SA2623N hosted by University Hasselt.

The computational resources and services used in this work were provided by the VSC (Flemish Supercomputer Center), funded by the Research Foundation - Flanders (FWO) and the Flemish Government.

This research was performed in the context of the Archer project. The Archer project was carried out by academic research partners UHasselt and KU Leuven in collaboration with the industrial partners EQUANS and Magics Instruments. This project is funded by the Energy Transition Fund of the FOD economy (federal government Belgium). The publication exclusively contains the opinions of the authors. The General Directorate Energy is not liable for any use of the information in the current paper.

References

[1] R. Volk, F. Hübner, T. Hünlich, F. Schultmann, The future of nuclear decommissioning – a worldwide market potential study, Energy Pol. 124 (Jan. 2019) 226–261.
[2] J. Kaulard, B. Brendebach, Radiation Protection during Decommissioning of Nuclear Facilities – Experiences and Challenges, vol. 70, 2005, pp. 14–24.
[3] D. De Schepper, I. Dekker, M. Simons, L. Brabants, W. Schroeyers, E. Demeester, ARCHER: autonomous robot platform for CHaractERization, IEEE Rob. Autom. Lett. (2022).
[4] Radiological Characterization of Shut Down Nuclear Reactors for Decommissioning Purposes, INTERNATIONAL ATOMIC ENERGY AGENCY, Vienna, 1998, p. 389.
[5] F. Jean, F. Lainb, C. Lbv, CARTOGAM portable gamma imaging 47 (3) (2000) 952–956.
[6] K. Amgarou, A. Patoz, D. Rothan, N. Menaa, iPIX: A New Generation Gamma Imager for Rapid and Accurate Localization of Radioactive Hotspots, 2014, pp. 3–5.
[7] C.G. Wahl, et al., The Polaris-H imaging spectrometer, Nucl. Instruments Methods Phys. Res. Sect. A Accel. Spectrometers, Detect. Assoc. Equip. 784 (Jun. 2015) 377–381.
[8] D. Turecek, J. Jakubek, E. Trojanova, L. Sefc, Compton camera based on Timepix3 technology, J. Instrum. 13 (11) (Nov. 2018) C11022. C11022.
[9] Y. Kim, T. Lee, W. Lee, Radiation measurement and imaging using 3D position sensitive pixelated CZT detector, Nucl. Eng. Technol. 51 (5) (2019) 1417–1427.
[10] M. Herranz, F. Aspe, K. Amgarou, Recommended in Situ Measurement Techniques for Each Constrained Environment, INSIDER, 2020 755554.
[11] K. Amgarou, M. Herranz, State-of-the-art and challenges of non-destructive techniques for in-situ radiological characterization of nuclear facilities to be dismantled, Nucl. Eng. Technol. 53 (11) (Nov. 2021) 3491–3504.
[12] V. Paradiso, K. Amgarou, N.B. de Lanaute, F. Bonnet, O. Beltramello, E. Liénard, 3-D localization of radioactive hotspots via portable gamma cameras, Nucl. Instruments Methods Phys. Res. Sect. A Accel. Spectrometers, Detect. Assoc. Equip. 910 (August) (2018) 194–203.
[13] D. Turecek, J. Jakubek, E. Trojanova, L. Sefc, Single layer Compton camera based on Timepix3 technology, J. Instrum. 15 (1) (2020) 17.
[14] T. Poikela, et al., Timepix3: a 65K channel hybrid pixel readout chip with simultaneous ToA/ToT and sparse readout, J. Instrum. 9 (5) (2014).
[15] M.J. Cree, P.J. Bones, Towards direct reconstruction from a gamma camera based on Compton scattering, IEEE Trans. Med. Imag. 13 (2) (1994) 398–407.
[16] ADVACAM, "PIXet Pro." (V1.7.8). available; https://advacam.com/downloads/..
[17] M. Khalil, D. Turecek, J. Jakubek, J. Kehres, E.S. Dreier, U.L. Olsen, Intrinsic XRF corrections in Timepix3 CdTe spectral detectors, J. Instrum. 14 (1) (Jan. 2019) C01018.
[18] R.D. Deslattes, et al., X-Ray Transition Energies, 2005 [Online]. Available:, version 1.2. http://physics.nist.gov/XrayTrans. Accessed: 08-Mar-2023.
[19] B. Bergmann, et al., 3D track reconstruction capability of a silicon hybrid active pixel detector, Eur. Phys. J. C 77 (6) (2017) 1–9.
[20] B. Bergmann, P. Burian, P. Manek, S. Pospisil, 3D reconstruction of particle tracks in a 2 mm thick CdTe hybrid pixel detector, Eur. Phys. J. C 79 (2) (2019).
[21] G. Arino-Estrada, et al., Measurement of mobility and lifetime of electrons and holes in a Schottky CdTe diode, J. Instrum. 9 (12) (Dec. 2014).
[22] J. Fink, H. Krüger, P. Lodomez, N. Wermes, Characterization of charge collection in CdTe and CZT using the transient current technique, Nucl. Instruments Methods Phys. Res. Sect. A Accel. Spectrometers, Detect. Assoc. Equip. 560 (2) (May 2006) 435–443.
[23] Q.-Y. Zhou, J. Park, V. Koltun, Open3D: A Modern Library for 3D Data Processing, Jan. 2018.
[24] D. Turecek, J. Jakubek, P. Soukup, USB 3.0 readout and time-walk correction method for Timepix3 detector, J. Instrum. 11 (12) (2016).
[25] E. Frojdh, et al., Timepix3: first measurements and characterization of a hybrid-pixel detector working in event driven mode, J. Instrum. 10 (1) (Jan. 2015) C01039.

[26] M. Urban, D. Doubravová, Timepix3: temperature influence on X-ray measurements in counting mode with Si sensor, Radiat. Meas. 141 (Feb. 2021) 106535.

[27] L. Brabants, G. Lutter, J. Paepen, B. Vandoren, B. Reniers, W. Schroeyers, Validation of TOPAS MC for modelling the efficiency of an extended-range coaxial p-type HPGe detector, Appl. Radiat. Isot. 173 (Jul. 2021) 109699.

[28] G. Daniel, O. Limousin, D. Maier, A. Meuris, F. Carrel, Compton imaging reconstruction methods: a comparative performance study of direct back-projection, SOE, a new Bayesian algorithm and a new Compton inversion method applied to real data with Caliste, EPJ Web Conf. 225 (2020) 06006.